5.0 Beam emission spectroscopy at JET

5.1 Historical overview

Observations of the D-α emission feature emitted by excited beam neutrals was first recorded at JET Joint Undertaking[59] and then subsequently studied on other fusion devices[60,61]. Due to the unique nature of the Stark resolved spectrum, the diagnostic application of the D-α beam emission feature provided a means of measuring a novel set of important plasma parameters[62]. Information regarding the internal magnetic field structure [61,63,64,65,66] and ion density fluctuations of the plasma [67,68] were the first quantities studied using beam emission spectroscopy .

However progress in exploiting the beam emission signal to obtain information on the neutral beam density was slow. The neutral beam density is an important plasma parameter which beam emission spectroscopy was envisaged to yield. It is a key piece of information required to validate the impurity content of the plasma deduced via charge exchange spectroscopy[69] and modelled beam stopping.

Prior to the discovery of the diagnostic implications of the beam emission signal, the neutral beam density could only be obtained from an attenuation calculation for the rate at which the neutral beam atoms were being ionised as the beam traversed the plasma. As discussed by von Hellermann[70] the accuracy of this method is limited by error amplification, particularly in high density plasma scenarios such as the anticipated operating regime of ITER[71]. Therefore the possibility of utilising the beam emission signal to provide a local accurate measurement of the neutral beam density was encouraging.

The first detailed attempt to exploit the beam emission signal following the initial work of Boileau[62] at JET was by Mandl[20,72]. Mandl explored the feasibility of utilising the beam emission spectrum to deduce the neutral beam density as well as other parameters such as the magnetic field strength, the divergence and energy composition of the beam as well as the location of the observation volume. His work focused on the beam emission signal originating from single beam bank pulses where the observed spectra, even though complicated, were in their simplest form. He suggested that it was possible to deduce the neutral beam density reliably for single bank pulses and that beam emission spectroscopy certainly had the potential to replace the numerical attenuation calculation. However single bank pulses only

constitute a minority of pulses at JET, high power double beam bank pulses are more common. Also Mandl's analysis, though fruitful, was in fact limited to just one pulse. The aim of the present work was to extend the analysis to include double beam bank scenarios.

Since the work of Mandl in 1991, the beam emission diagnostic had been relocated to a different observation port. The status of the diagnostic after the appropriate modifications were implemented was such that the neutral beam density inferred from the beam emission spectra differed from the values obtained from the numerical attenuation calculation, in many cases by up to a factor of two. This was such a contrast to the original results reported by Mandl that there was an obvious need to revisit each stage of the analysis to investigate the nature of the discrepancy.

In this work we address this issue while focusing our attention on the analysis of the beam emission spectra originating from single and double beam bank pulses.

5.2 The JET beam emission spectroscopy diagnostic

5.2.1 Diagnostic apparatus

The beam emission spectrum at JET is recorded using a back illuminated CCD camera. A fan of twelve fibre optics are focused along the trajectory associated with injectors 6 and 7 of octant eight from the diagnostic port illustrated in figure 5.1. Injectors 6 and 7 are members of the normal and tangential bank respectively and conveniently share a similar trajectory as can also be seen in figure 5.1. Each of the twelve fibre optics are employed to relay the D-α emission feature back to a Czerny-Turner type spectrometer (KS5b). On leaving the exit slit of the spectrometer the emission feature is then focused onto the CCD camera. The signals recorded by the camera are then collected and stored awaiting analysis. A schematic overview of the diagnostic system is shown in figure 5.2 and a detailed description can be found in [66] and references therein.

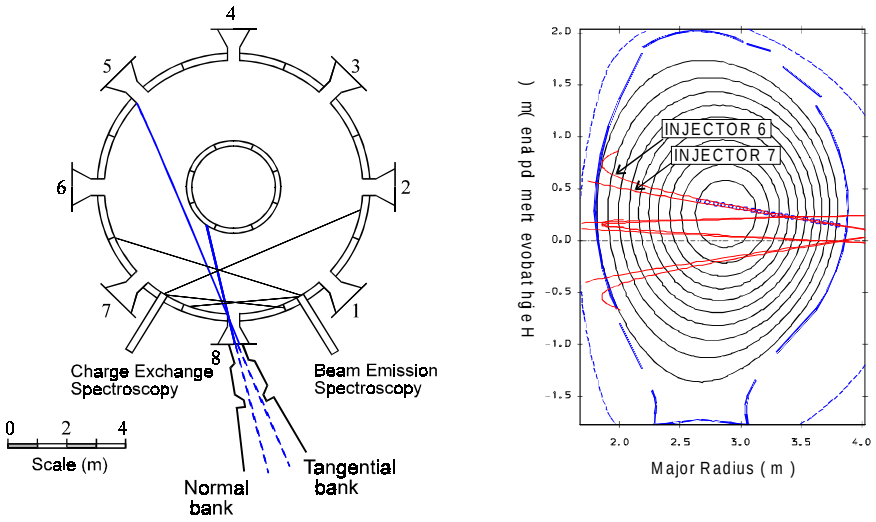

Figure 5.1 Plan view and side elevation of the tokamak. The figure on the left illustrates the location of the observation ports for charge exchange and beam emission spectroscopy. The figure on the right shows the typical trajectories of each neutral injector, particular attention should be drawn to the diagnostic injectors 6 and 7 which are annotated.

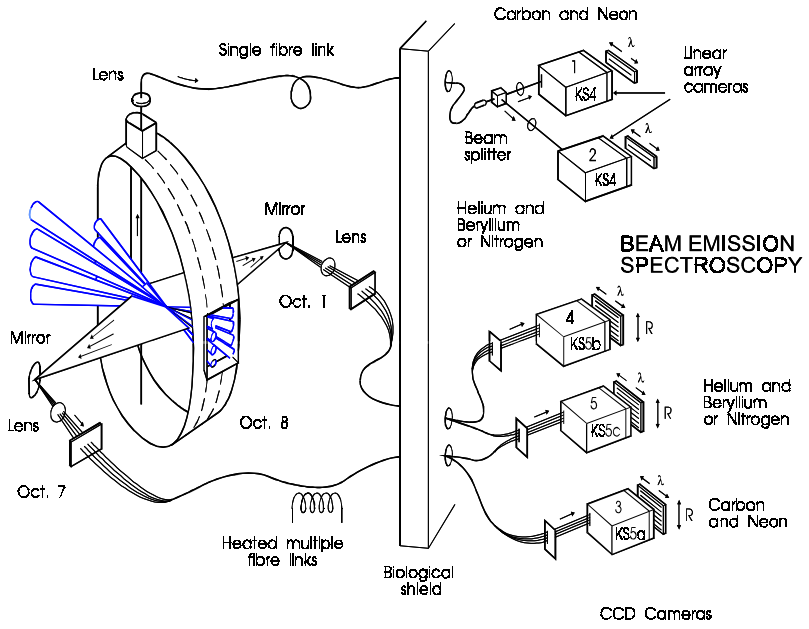

Figure 5.2 Schematic overview of the diagnostic system employed to measure both the neutral beam density and the impurity content of the plasma. Situated on octant one, a fan of twelve fibre optics focused along the trajectory of the neutral beams are used to relay the D-α emission feature back to a Czerny-Turner type spectrometer (KS5b). On leaving the exit slit of the spectrometer the emission feature is recorded via a back illuminated CCD camera.

5.2.2 Observed beam emission spectrum

The primary beam emission observation is of a series of overlapped Doppler shifted Stark multiplet features. The appearance of the 6560 - 6620 Å spectral interval for a single bank pulse is shown in figure 5.3,

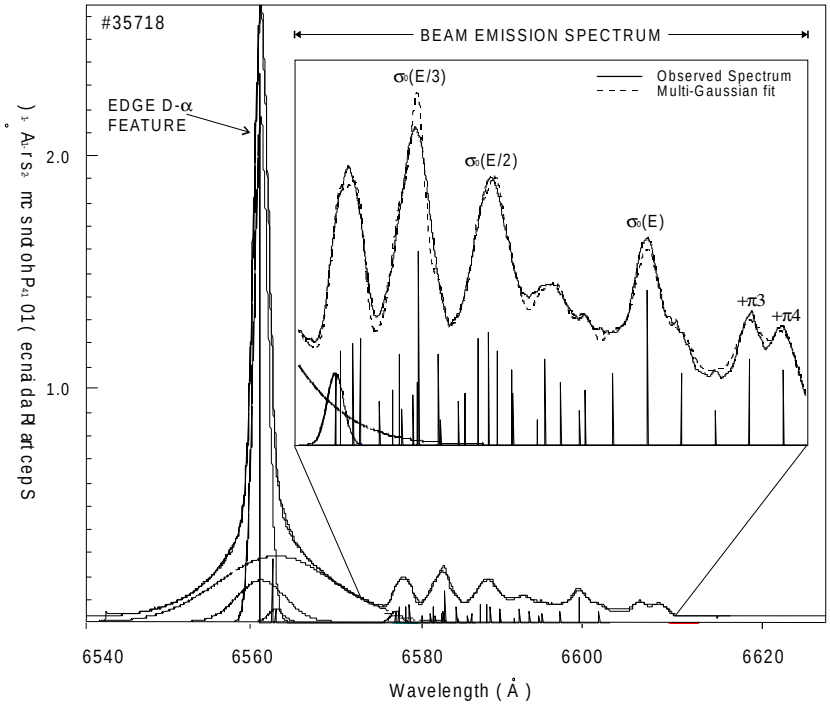

Figure 5.3 Observed motional Stark D-α feature. The emission feature was recorded during the JET pulse 35718 using track 4 of the multichord system. The tangential bank was active with a primary energy of 140 KeV/amu. The constrained multi-gaussian fit is also shown. Particular attention should be brought to the annotation of the full, half and third σ_0 Stark components. Due to the existence of the three fractional energy components in the beam this gives rise to three Stark multiplets. Each Stark multiplet is Doppler shifted according to the velocity of the relevant beam neutrals and as a result the overall picture is an overlap of each Stark feature.

where only one diagnostic neutral injector ('pini') is active. The existence of three fractional energy components in each diagnostic injector gives rise to three Stark multiplet features. Each Stark multiplet is Doppler shifted according to the velocity of the relevant energy component and the viewing angle between the neutral injector and the line of sight. The fractional energy components in each injector are due to the production of D^+ , D^+_2 and D^+_3 during ion generation[73]. As the ions are neutralised their different atomic masses contribute to producing three energy components, i.e. a full energy E_0, half energy $E_{0/2}$ and a third energy $E_{0/3}$ component.

The salient features of the spectrum as we move in the direction of increasing wavelength commences with the large D-α edge emission line situated at 6560 Å. The origin of this is the presence of partially ionised species between the last closed magnetic flux surface and the vessel wall. Next we encounter a cluster of Stark multiplet features which are collectively known as the beam emission spectrum. Each Stark multiplet feature consists of nine observable Stark components (up to $\pm\pi 4$). The higher order components of the Stark resolved spectrum are too weak in intensity to observe reliably.

The beam emission spectrum is highly determined. The local magnetic field orthogonal to the neutral beam particle path together with precisely known velocities of the energy fractions determines the wavelength separation of the Stark components. The relative intensities of the σ and π polarisation components are also determined since Stark fine structure populations are fully mixed at the JET core plasma densities ($> 2 \times 10^{13}$ cm^{-3}) and the geometry is specified.

In the case of double beam bank pulses, which are more common, the recorded beam emission spectrum originates from the excited beam neutrals of two diagnostic injectors so that the spectrum comprises of six overlapping Stark multiplet features. In figure 5.4, the beam emission spectrum during the single bank period of the pulse 32969 showing the three Stark multiplets increases in complexity suddenly during the double beam bank period of the pulse.

In both the single and double bank spectra, additional spectral lines in the vicinity of the beam emission spectrum can also be observed, particularly near the base of the D-α edge emission line, see figure 5.3. Our concern here however is with the Stark multiplet features of the beam emission spectrum (see [20] for a detailed description of the full spectrum) .

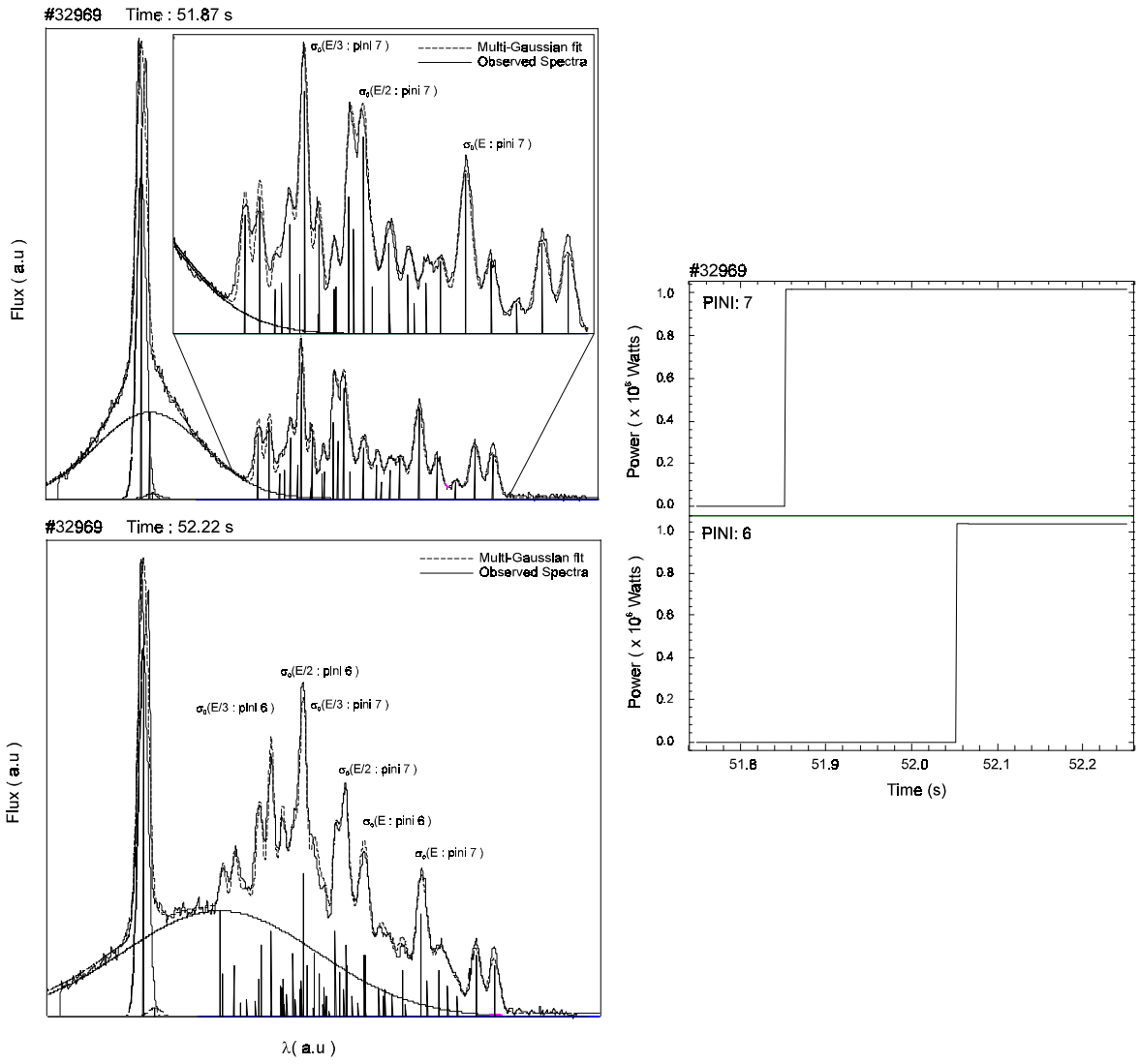

Figure 5.4 Complexity of the beam emission signature. Top left hand figure shows the beam emission feature during a single bank period of the pulse 32969. The figure at the bottom left illustrates the increasing complexity of the observed spectrum during the double beam bank period. The single figure to the right shows the power associated with each diagnostic injector and the time interval when the single or double bank scenario is in operation.

5.2.3 Experimental analysis

5.2.3.1 Method and objectives

The analysis of the beam emission feature involves generating a synthetic model spectrum based on measured and calculated parameters. The synthetic spectrum is then employed to extract the total flux associated with each Stark multiplet contained within the spectrum. The total flux together with knowledge of the electron density

and the effective beam emission coefficient enables the neutral beam density to be recovered from the beam emission spectrum. At JET a computer program written in FORTRAN 77 is employed to automate the spectral analysis. The program was originally written by Mandl[20] and extended by English[74] and Howman[75] to include the analysis of the spectral originating from the excited neutrals of two active injectors. The procedure consists of two stages as illustrated in figure 5.5.

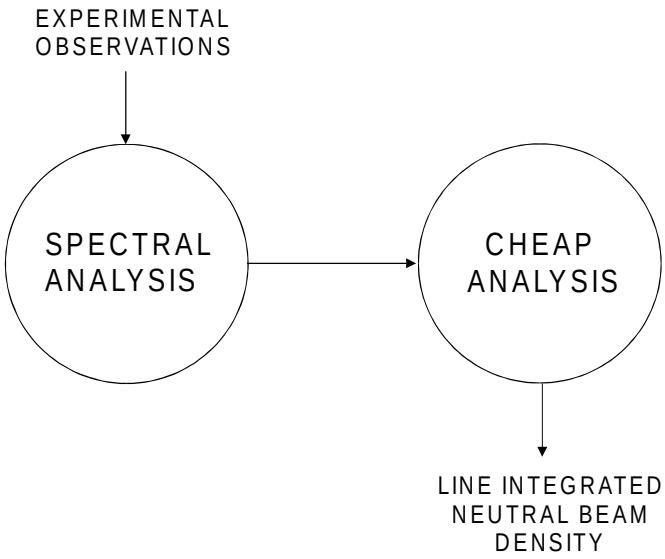

Figure 5.5 Overview of the two stage procedure involved in obtaining the line integrated neutral beam density. The first stage involves running the spectral analysis code to obtain the total flux from each Stark multiplet. The second stage of the analysis involves evaluating the neutral beam density using the flux measurements together with derived atomic data.

The first stage uses the spectral analysis program to extract the total flux associated with each Stark multiplet. The second stage is a post processing step. The post processing code, which is known as the Charge Exchange Analysis Package (CHEAP), evaluates the neutral beam density using the flux measurements. The CHEAP code was written in FORTRAN 77 by von Hellermann[59] and serves as the main analysis tool for the core spectroscopy group at JET (see section 5.3).

5.2.3.2 Motional Stark Effect

The motional Stark effect is the descriptive name for the Stark effect when atoms move through a magnetic field and experience a Lorentz electric field within their own frame of reference. The Lorentz electric field acts as a perturbation on the atom’s

Hamiltonian and influences the wavelength and intensities of the emission. Neutral deuterium beam atoms, which cross the confining magnetic field of the JET tokamak with a typical velocity of around 10^6 m s^{-1}, experience an electric field of up to 10^6 Vm^{-1}. In this regime the linear Stark effect is dominant and the influence of the electric field removes the degeneracy associated with each hydrogenic energy level. This gives rises to a Stark resolved energy level structure where the splitting of the energy levels is directly proportional to the electric field. As discussed by Sobelman[76] the splitting of the energy levels are given by,

$$\Delta E = \frac{3}{2} n(n_1 - n_2) e E_L a_0 \qquad 5.1$$

where n_1 and n_2 are the so-called parabolic quantum numbers and E_L is magnitude of the Lorentz electric field. In figure 5.6 we show a schematic for the transition from a degenerate energy level structure to a Stark resolved picture for neutral hydrogen. Also shown are the expected emission patterns.

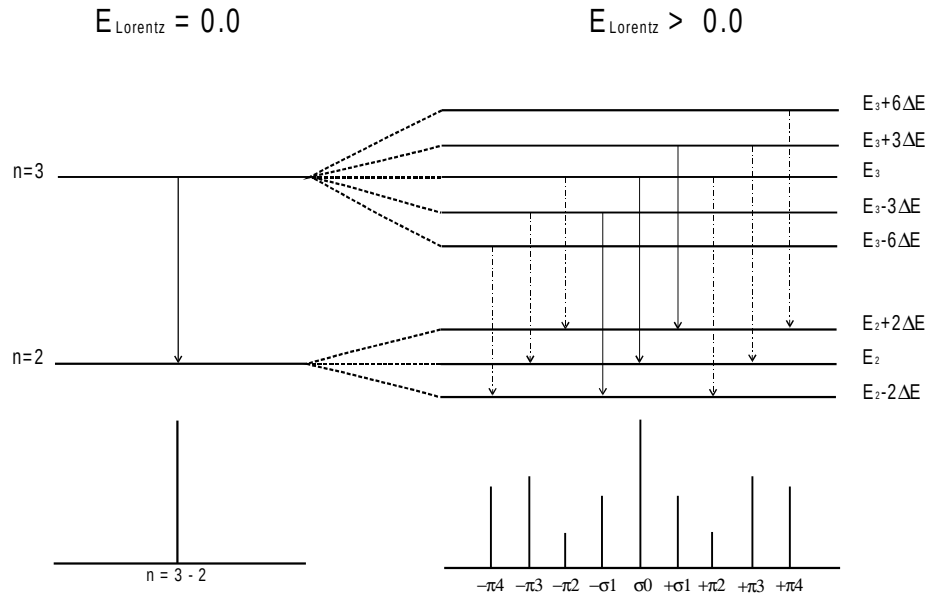

Figure 5.6 Influence of an external electric field on the degenerate energy levels of hydrogen. The electric field acts as a perturbation and removes the degeneracy associated with each energy level and gives rise to a Stark resolved energy level structure. The schematic illustrates the transition from a degenerate energy level structure to a Stark resolved picture showing the subsequent emission patterns.

5.2.3.3 Spectral analysis

The analysis of the beam emission spectrum involves identifying the position and amplitude of every feature contained within the spectrum region. Each feature is then represented by a Gaussian specified by width and amplitude. The array of Gaussians which collectively represent all of the individual spectral features is then used to construct a synthetic spectrum which is adjusted to extract the flux associated with each Stark multiplet.

The analysis program first accesses the JET pulse process file database system[77] to ascertain the atomic mass and velocity of the beam species. The program then searches the spectrum for the D-α edge emission line. Since this emission originates from the edge of the vessel it is free of any Doppler shift from the bulk motion of the plasma. It is utilised as a wavelength reference.

The spectral analysis code then attempts to locate the position of the Doppler shifted primary σ_0 Stark components associated with each Stark multiplet. The position of each primary Stark component is determined by the velocity, v_b, of the relevant energy fraction and the viewing angle, α, between the neutral injectors and the line of sight. Mandl[20] expresses the Doppler shifted wavelength as,

$$\Delta\lambda_{DOPPLER} = \lambda_0 \frac{v_b}{c}\cos(\alpha) \qquad 5.2$$

where λ_0 is the natural wavelength.

The location of the remaining Stark components for each multiplet are identified by assuming the Stark splitting is constant over the spectral region. The Stark splitting is then evaluated using the following expression,

$$\Delta\lambda_{STARK} = \frac{3}{2}\frac{ea_0}{hc}\lambda^2 E_L \qquad 5.3$$

where λ is the unperturbed wavelength. The analysis program obtains estimates for the electric field using the results from magnetic equilibrium calculations[78] together with knowledge of the beam velocity and experimental geometry. The position of the components are then specified relative to the appropriate Doppler shifted primary Stark feature, as illustrated in figure 5.7 for a single multiplet.

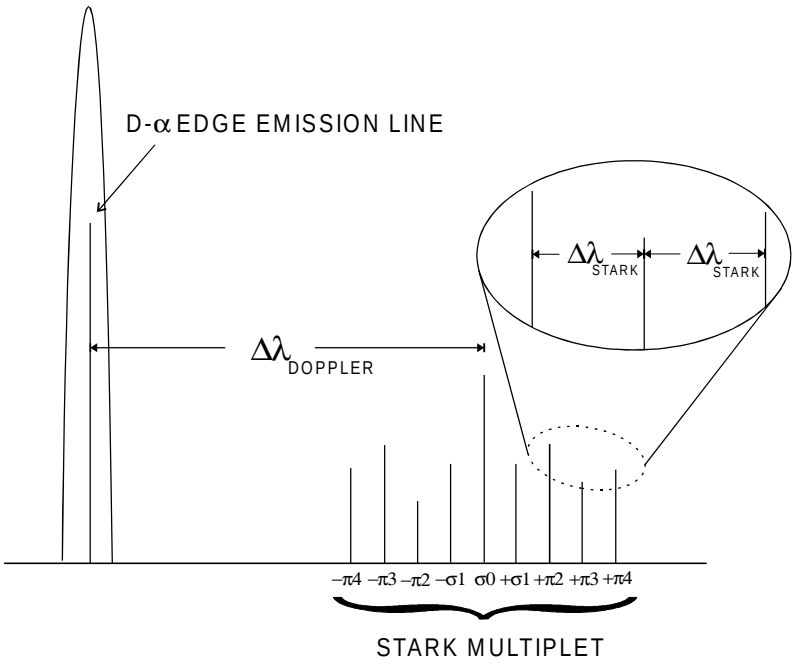

Figure 5.7 Schematic illustration of how the primary Stark component for a single multiplet feature is fixed relative to the D-α edge emission line and the remaining Stark components are then specified relative to the primary Stark component by the wavelength separation due to the linear Stark effect.

The next step for the analysis program is to obtain amplitudes for the Guassians used to represent each spectral feature. The amplitudes of the Gaussians for the primary σ_0 Stark components in both single and double bank spectra are treated as the search parameters of the fit, whilst the amplitudes of the Gaussians for the remaining Stark features are specified by a parametric relationship to the σ_0 components. This relationship is based on intensity ratios of individual Stark components which are entered by the user as input[74].

The resulting parameterised array of Gaussians is optimised by the NAG routine E04UPF to obtain a best fit synthetic spectrum to the experimentally observed spectrum. The degree of accuracy of the fit is monitored and after each spectrum is analysed a diagnostic report is automatically written to a file which includes the NAG error flag for the success of the fitting procedure[79]. It should be noted that the analysis program also addresses the spectral lines which can be observed near the base of the D-α edge emission feature.

5.3 The Charge Exchange Analysis Package

5.3.1 The role of the charge exchange analysis package

The charge exchange analysis package (CHEAP) is a computational tool employed at JET to automate the process of combining spectroscopic observations, derived atomic data and experimental conditions to infer self consistently various plasma parameters. The main application of CHEAP is the deduction of absolute impurity concentrations via charge exchange emission measurements, which are recorded using the apparatus shown in figure 5.2.A schematic overview of CHEAP illustrating the flow of derived atomic data and experimental observations is shown in figure 5.8

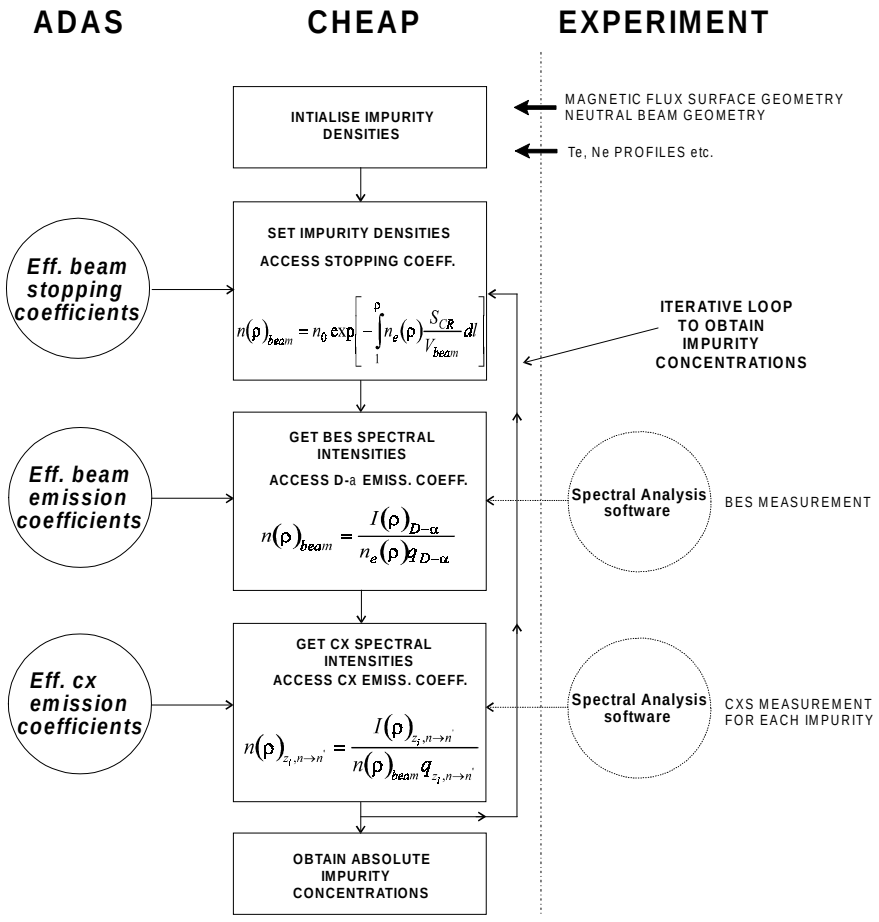

Figure 5.8 Schematic overview of the Charge Exchange Analysis Package, CHEAP. The deduction of the impurity content of the plasma within CHEAP involves utilising charge exchange emission flux measurements together with derived atomic data. The assembly of the neutral beam density using the

flux measurements from the beam emission signal as well as the attenuation calculation is carried out within CHEAP.

5.3.2 Iterative path to absolute impurity concentrations

The charge exchange spectroscopy diagnostic at JET utilises the subsequent emission by impurity ions following the capture of an electron to obtain information on the impurity content of the plasma. The impurity concentration of a species of nuclear charge z_0, as discussed in chapter 1.0, is given as

$$n_{z_0} = \frac{4\pi \int \Phi_{CX}(\lambda) d\lambda}{q_{cx} \int n_b ds} \qquad 5.4$$

where Φ_{cx} is the recorded charge exchange flux, q_{cx} is the effective charge exchange emission coefficient[19] and $\int n_b ds$ is the line integrated neutral beam density.

Evaluation of the line integrated neutral beam density from either the attenuation calculation or the beam emission spectrum requires prior knowledge of the impurity densities in the plasma to enable the relevant effective coefficients to be evaluated. This requires an iterative approach for the concentration of the different impurities in the plasma to be inferred via charge exchange spectroscopy. The CHEAP package implements such an iterative calculation making use of bremsstrahlung and charge exchange flux measurements together with derived atomic data, see figure 5.8. To reconstruct the radial density profiles for each impurity CHEAP begins by estimating the impurity content of the plasma. This estimate is obtained from the bremsstrahlung observations along the vertical line of sight shown in figure 5.2. The measurement enables the line integrated effective ion charge of the plasma to be inferred using the following equation[80],

$$\left\langle Z_{eff} \right\rangle = \frac{1}{B}\left[\frac{\pi k}{2m}\right]^{\frac{1}{2}} \phi_{brems} \Big/ \int \frac{n_e^2}{\sqrt{T}} \frac{g^{III}}{\lambda} \exp\left[\frac{E_v}{kT}\right] dl \qquad 5.5$$

where g^{III} is the free-free Gaunt factor and ϕ_{brems} is the intensity of the emission. It is then assumed that the contribution to the bremsstrahlung emission is due to the

presence of only one impurity in the plasma. This is the dominant impurity (normally known) such as carbon. The value obtained for $< Z_{eff} >$, is then used as a first approximation in the following expression for the local ion charge, Z_{eff}.

$$Z_{eff} = 1 + \sum_i Z_i (Z_i - 1) \frac{n_i}{n_e} \qquad 5.6$$

This enables the carbon concentration to be estimated. Measurements of the bremsstrahlung emission are repeated. This time the contribution to the emission is assumed to be due to the presence of carbon and an additional impurity. The impurity density for each species is thus calculated using the first estimate for the carbon concentration as a starting point. This procedure is continued until all the main impurities have been included and a stable solution for the vertical line of sight has been obtained.

The reconstruction of the radial density profiles can now be considered. The present implementation of CHEAP employs the theoretical attenuation calculation to evaluate the neutral beam density during the analysis. Using the values for the impurity content of the plasma obtained from the vertical line of sight as an initial guess, the effective stopping coefficients are evaluated to obtain the neutral beam density. Together with knowledge of the neutral beam density and the charge exchange flux measurements a new set of values for the impurity content of the plasma can be calculated. These are then used to evaluate new stopping coefficients and the process continues until a converged solution for the impurity concentrations has been achieved.

5.3.3 Evaluation of the neutral beam density

An efficient method to calculate the neutral beam density is required for the impurity concentrations to be deduced within a reasonable time scale. This is done by acquiring the theoretical data through the linear interpolation and combination method with look up tables as discussed in chapter 4.0.

5.3.3.1 Numerical attenuation calculation

Utilising the rapid look up tables of type adf21, the CHEAP code assembles effective stopping coefficients for a composite plasma as a function of temperature, density and neutral beam energy (T_e, n_e and E_b). In the case of a single injector the neutral beam density as a function of radial position, ρ, can then be obtained using the following relation,

$$n(\rho)_b = n_0 \exp(-\int_1^{\rho} n_e \frac{S_{CR}(n_i, E_b, T_e)}{v_b} dl) \qquad 5.7$$

where dl is along the path taken by the neutral beam, S_{CR} is the effective stopping coefficient in terms of the ion density, and n_0 is the initial beam density on entry to the plasma.

For charge exchange spectroscopy, we require the line integrated neutral beam density i.e. $\int n_b ds$, where ds is along the line of sight across the neutral beam profile. Test bed measurements[81] show that the neutral beam density distribution at JET can be described by a Gaussian which has a full width half maxima (FWHM) in the x and y plane of w_x and w_y respectively, see figure 5.9.

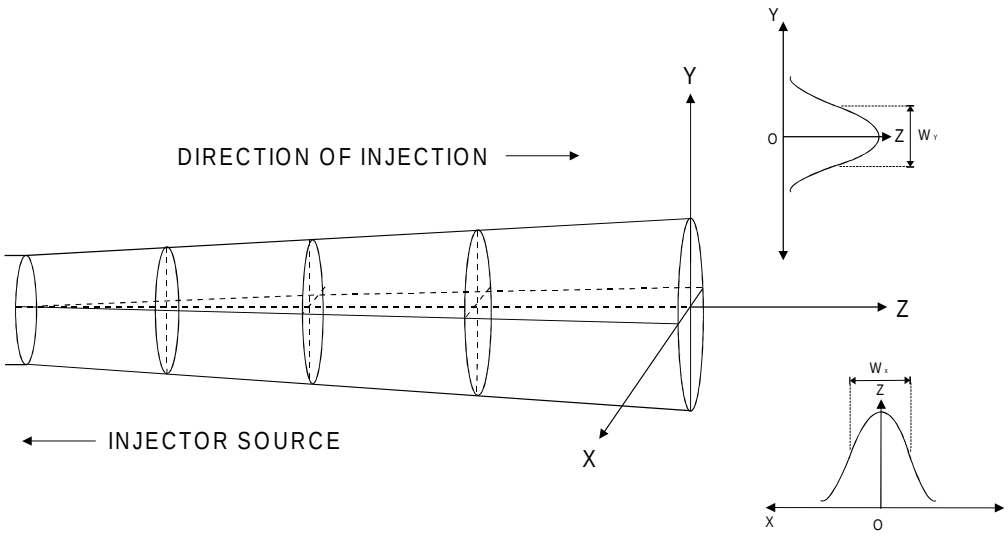

Figure 5.9 An illustration of a single beam showing the natural beam divergence . Also shown is the Gaussian distribution in both the x and y plane which is used to describe the neutral beam density distribution of the beam.

Therefore the line integrated neutral beam density evaluated by CHEAP is,

$$\langle n(\rho)_b \rangle = \int n(\rho)_b ds = n_0 \int_{-\infty}^{+\infty} \exp(-\frac{x^2}{w_x^2} - \frac{y^2}{w_y^2}) \exp(-\int_1^{\rho} n_e \frac{S_{CR}(n_i, E_b, T_e)}{v_b} dl) ds \qquad 5.8$$

The FWHM of the Gaussian in the x and y plane at any radial position is obtained by assuming that the beam source is a point[81]. The values for the beam divergence can then be used to obtain the widths, w_x and w_y. The electron density is obtained from Thomson scattering measurements from the LIDAR diagnostic[82]. The initial beam density, n_0, is obtained from calorimetry measurements of the beam current in the neutral injector[83].

5.3.3.2 Spectroscopic measurement

The CHEAP code employs the look up tables of type adf22 to assemble effective beam emission coefficients for a composite plasma. The relationship between the beam emission flux and the line integrated neutral beam density as evaluated by CHEAP for a single injector is,

$$\langle n(\rho)_b \rangle = \frac{\chi}{n_e(\rho)} \sum_{k=1}^{k=3} \frac{I(E_{0k})}{q(n_e, T_e, E_{0k})_{D-\alpha}} \qquad 5.9$$

where $I(E_{0k})$ is the flux associated with the Stark multiplet corresponding to the fractional energy component k , $q(n_e,T_e,E_{0k})$ is the effective D-α beam emission coefficient and χ is the window transmission factor. The latter is used to compensate for the observation window being optically degraded by the deposition of impurities. It is evaluated by comparing the $< Z_{eff} >$ inferred from the bremsstrahlung measurements recorded from the charge exchange diagnostic port and the vertical line of sight as shown in figure 5.2. The observation port for the vertical line of sight is a considerable distance away from the plasma and the window is assumed to be free of any optical degradation. A detail discussion of the cross calibration technique is given by Morsi et. al.[9].

5.4 Examination of the analysis procedure

5.4.1 Overview

To address the nature of the discrepancy between the neutral beam density inferred from the numerical attenuation calculation and the beam emission signature, a systematic approach was adopted which involved investigating each stage of the analysis. There were three areas of uncertainty, namely the spectral analysis, the CHEAP analysis and the derived atomic data. Our strategy involved investigating each area in turn in an attempt to identify the source of the discrepancy.

5.4.2 The spectral analysis

Due to the large quantity of spectral data to be analysed on a daily basis at JET, the spectral analysis program operates in a batch mode. In this mode the program automatically analyses every spectrum recorded over the duration of a particular pulse selected by the user.

To operate the analysis code in this manner involved configuring the input parameters to ensure that the synthetic spectra generated by the code would give an accurate fit to all of the recorded spectra. In practise this was achieved by considering a few spectra from different time frames and lines of sight. It was then assumed that the optimum input parameters obtained would then be valid for the analysis of all the other spectra.

We found that some of the spectra were not being fitted to the required accuracy. The acceptance criteria of the goodness of fit from the NAG algorithm was to loose. The failure rate was sensitive to poor input parameter choice such as ignoring the variability between different lines of sight. Also the temporal variation of the CII passive emission lines which pollute the beam emission signal, see figure 1.5, were not taken into account. During observations the intensity of these lines would unpredictably become stronger or weaker and directly influence the success of the fitting procedure. The obvious solution would be to check each spectrum individually but this would be impractical due to the large volume of data. An alternative approach was sought.

In all of the spectra associated with single bank pulses, it was observed that the $+\pi 3$ and $+\pi 4$ Stark components of the full energy fraction were separated from the

dense cluster of Stark lines, see figure 5.3 . As suggested by Howman[75], the fit could be biased in favour of these two components (while neglecting the remaining features) and together with knowledge of the intensity ratios of the remaining Stark components, the total flux associated with the full energy fraction could be reconstructed. The total flux for the Stark multiplet feature due to the full energy fraction of a single injector, assuming that the feature is symmetrical around the primary σ_0 component, is given as,

$$\Phi_{Total} = 2\left[\phi_{\pi 3} + \phi_{\pi 4}\right] + 2\left[\phi_{\pi 2} + \phi_{\sigma 1}\right] + \phi_{\sigma_0} \qquad 5.10$$

This expression can be reduced to a simple relation involving the measurement of the flux associated with only the $+\pi 3$ and $+\pi 4$ Stark components,

$$\Phi_{Total} = \kappa\left[\phi_{\pi 3} + \phi_{\pi 4}\right] \qquad 5.11$$

where κ is a constant obtained from the intensity ratios of the remaining Stark lines.

The contribution to the neutral beam density due to the full energy fraction could be recovered from the spectrum while reducing the number of spectral features which are taken into account. To obtain the contribution to the neutral beam density from the remaining fractional energy components, Howman[75] suggested that one could use the following relation.

$$N^{Measured}_{E_0/k}(\rho) = \frac{N^{Theory}_{E_0/k}(\rho)}{N^{Theory}_{E_0}(\rho)} N^{Measured}_{E_0}(\rho) \qquad 5.12$$

where $N^{Theory}_{E0/k}$ is the contribution to the total beam density due to the fractional energy component k, which is obtained from the attenuation calculation. $N^{Measured}_{E0}$ is the contribution to the total neutral beam density due to the full energy fraction which is obtained from the $+\pi 3$ and $+\pi 4$ Stark components.

This method could also be extended to include the analysis spectra associated with double beam bank pulses. In which case the line ratios of the Stark components are assumed to be identical for each bank and the reconstruction of the flux associated with each full energy component is carried out in the same manner.

As part of a feasibility study we implemented this method in an attempt to improve the reliability of the spectral fitting . To obtain a value for κ we conducted a

statistical survey of the experimental data from which we obtained the line ratios shown in table 5.1, also shown in the table are the theoretical values predicted by Mandl[20].

Ratio	*Experimental*	*Theoretical*
σ_1/σ_0	0.430	0.353
π_3/σ_0	0.550	0.421
π_2/σ_0	0.195	0.133
π_4/σ_0	0.450	0.307

Table 5.1 Experimental and theoretical line intensity ratios of the Stark components. The experimental values were obtained from a statistical analysis of the observed spectra. The theoretical values were obtained from the work of Mandl[20].

Using the values contained in table 5.1, this gave κ a value of 3.625 .We conducted a detailed study of the analysis using the $+\pi 3$ and $+\pi 4$ components to conclude that it was more reliable than the existing method. The existing method which involved extracting the flux associated with each individual Stark component is more applicable when the analysis of the spectra is done on an interactive basis rather than in a batch mode. We decided to continue the $+\pi 3$ and $+\pi 4$ method on a permanent basis. Nonetheless by adopting this new approach we have lost important diagnostic information concerning the half and third energy components. We had originally planned to used the fractional Stark components to verify the energy dependence of the effective emission coefficients and hence the fundamental cross section data. This opportunity is no longer available.

5.4.3 The CHEAP analysis

The CHEAP package utilises a vast amount of derived atomic data and anxieties regarding the correct use of the atomic data was of immediate concern. A careful study of CHEAP revealed an error in the implementation of the linear combination

method. This was corrected. This error did not have any significant impact on the discrepancy between the measured and calculated beam density.

5.4.4 Review of the fundamental and derived atomic data.

In this section we summarise the results obtained by reviewing the fundamental atomic data which is used as input to calculate the effective stopping and emission coefficients. Due to the energy regime of the JET heating beams, the ion-atom collisions govern the population structure and hence the attenuation. Therefore we restricted ourselves to the fundamental atomic data concerning ion-atom collisions.

The atomic database containing ion-atom collision cross sections, which is of the ADAS data format of adf02, was constructed in 1989 and periodically updated until 1993. Using the best available data we updated this data base, a detailed account can be found in appendix A. As an example we contrast the new 1997 cross-section data for ion impact ionisation from the n=3 shell of the beam neutrals with the 1989 data, see figure 5.10. At the operating densities of the JET tokamak, the role of ionisation from the excited states of the beam atoms is significant. A point to note is that the new 1997 database contains more accurate cross-sections for atomic processes associated with excited states which were not available when the 1989 database was compiled.

Using the new ion-atom collision database we then calculated new effective stopping and emission data for all of the fully stripped impurities up to the first period. In Figure 5.11 and 5.12 we illustrate the influence of the revised ion-atom collision data on both the effective Balmer-alpha emission coefficient and the line integrated neutral beam density deduced from the beam emission spectrum.

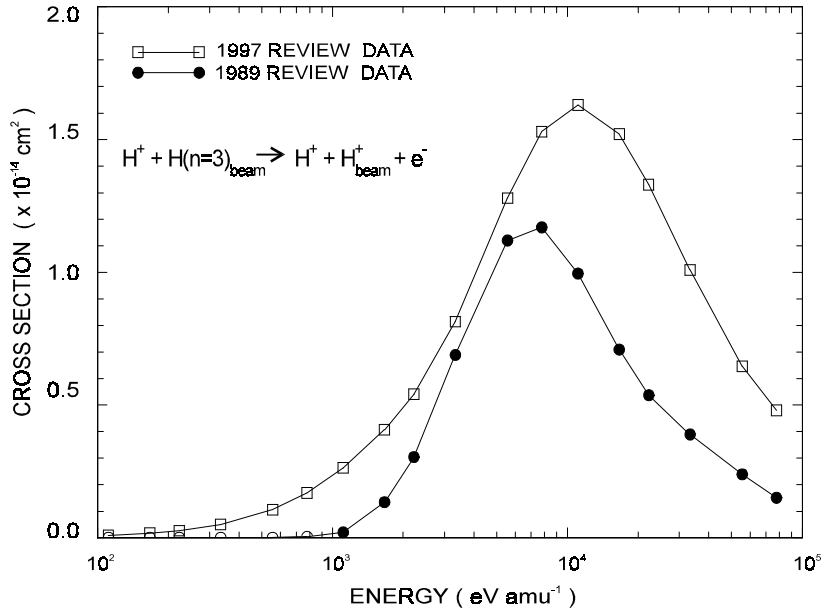

Figure 5.10 Ion impact ionisation cross section Vs energy. The 1997 data is based on the data compiled by Janev & Smith [Janev R K, Smith J J, J. Nucl. Fusion (Supplement), Vol.4,1993].

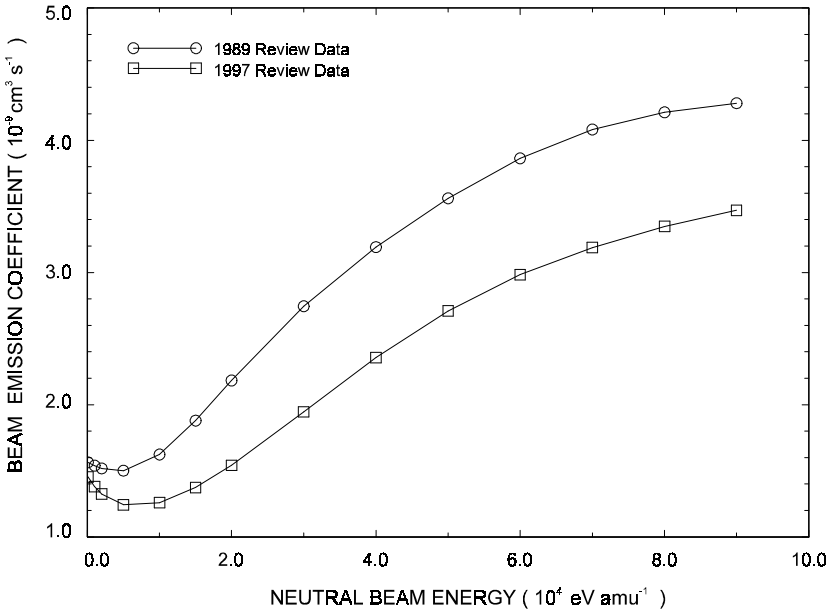

Figure 5.11 The Balmer-alpha effective emission coefficient for a pure D^+ plasma calculated using the 1989 and 1997 ion-atom collision database. The electron temperature is 1 x 10^3 eV and the electron density is 1 x 10^{13} cm^{-3}.

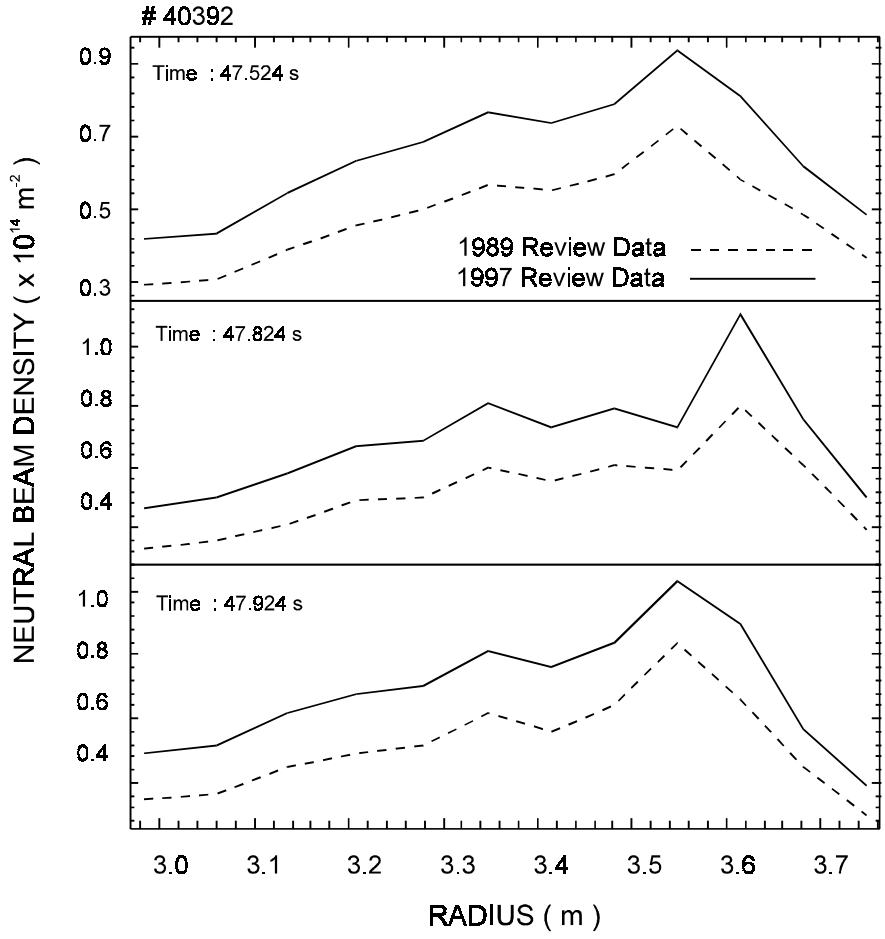

Figure 5.12 Line integrated neutral beam density for three different time periods obtained from the beam emission signal. The plot shows the direct influence of the fundamental data on the effective emission coefficient and hence the line integrated neutral beam density.

As can be observed from figure 5.11, the influence of the fundamental data on the effective Balmer-alpha coefficient is substantial. Using the new effective emission coefficients an average change of approximately 30 % in the neutral beam density inferred from the beam emission spectrum can be seen in figure 5.12.

We now illustrate the influence of the revised ion-atom collision data on the effective stopping coefficient and the line integrated neutral beam density obtained from the attenuation calculation, see figures 5.13 and 5.14 respectively.

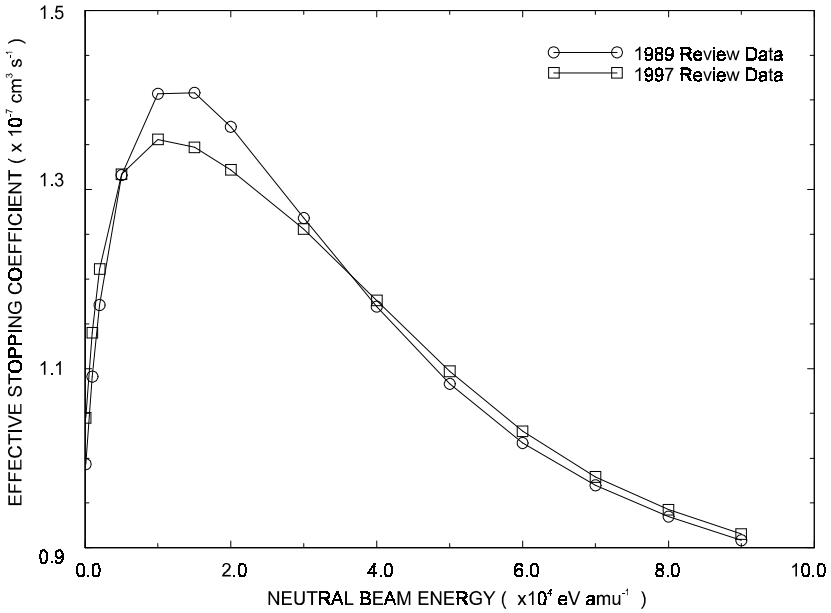

Figure 5.13 Comparison between the effective stopping coefficients calculated using the 1989 and 1997 ion-atom collision database. The plasma density was 1.0 x 10^{13} cm^{-3} and the temperature was 1.0 x 10^{3} eV. As can be observed the change with the revised 1997 data is small.

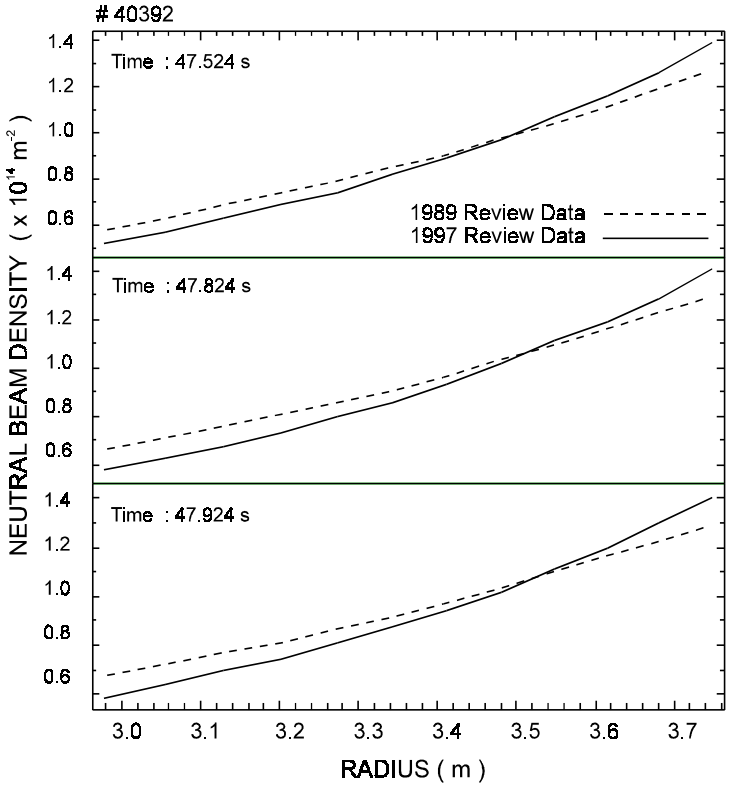

Figure 5.14 The line integrated neutral beam density for three different time periods evaluated using the attenuation calculation with the 1989 and 1997 data.

As can be seen in figure 5.13, the influence of the revised atomic data on the effective stopping coefficient and hence the line integrated neutral beam density obtained from the attenuation calculation is small, see figure 5.14. The new 1997 ion-atom collision database includes more accurate cross sections describing the atomic processes associated with the excited states. The changes in such cross sections contributes very little to the effective stopping coefficients since less than 1% of the beam neutrals are in their excited state, see figure 5.15.

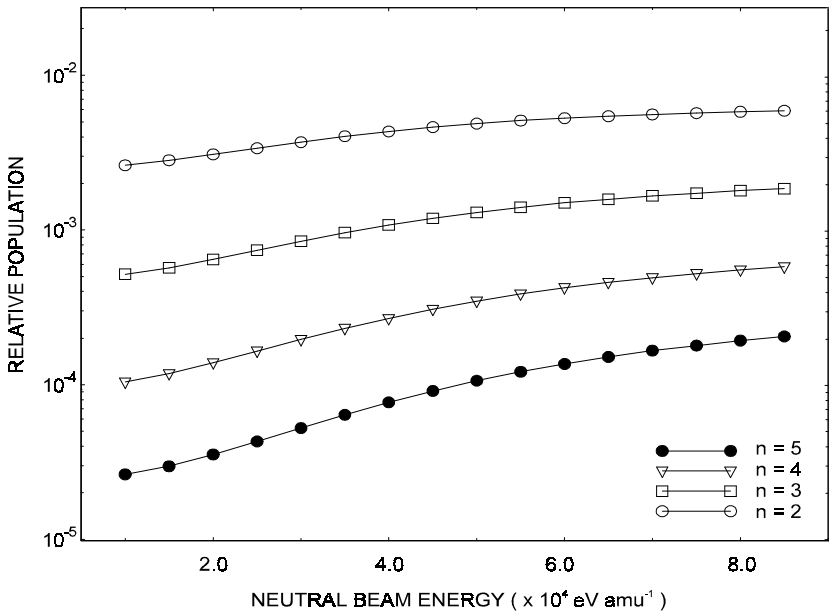

Figure 5.15 Population of the excited states relative to the ground state of the beam neutrals for a pure D^+ plasma. The plasma density and temperature are respectively 6 x 10^{13} cm^{-3} and 2 keV. As can be observed the population of the excited states is less than 1% of the ground population.

5.4.5 Conclusion

The original approach of analysing the beam emission spectrum by fitting all the Stark components proved to be unreliable when done in an unsupervised batch mode. A more reliable method was implemented which relies on reconstructing the flux from a fit of only the $+\pi 3$ and $+\pi 4$ components.

The review of the fundamental atomic data has led to a more accurate description of the behaviour of the atomic processes associated with the excited states. The revised atomic data has a substantial influence on the effective emission coefficients and hence the neutral beam density obtained from the beam emission

spectrum. The revised data had a much smaller effect on the effective stopping coefficients and hence the attenuation calculation.

5.5 Results

In this section we show separately the results obtained from the analysis of spectra recorded during single and double beam bank pulses. In both cases we compare the measured beam density with the values obtained from the numerical attenuation calculation. In each case we first illustrate the typical radial and time dependence of the measured and calculated neutral beam density. We then show the pulse to pulse variation between the results obtained from both methods.

5.5.1 Single beam bank pulses

In figure 5.16 we illustrate at three different time periods the behaviour of the radial dependence of the measured and calculated neutral beam density for a typical pulse.

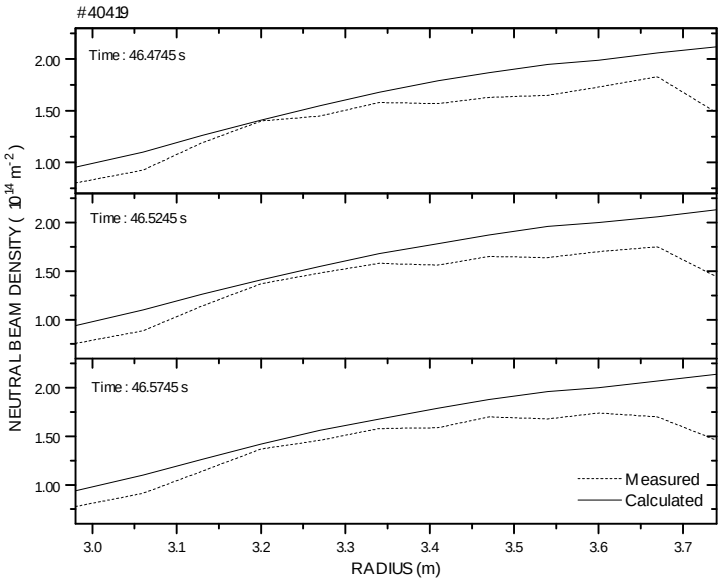

Figure 5.16 Radial dependence of the measured and calculated neutral beam density for the single beam bank pulse 40419. Three time slices have been selected to illustrate the results. A characteristic feature which can be observed in the majority of pulses is the fall off of the measured beam density as we move towards the edge (~ 3.7 m).

There is generally good agreement between the measured and calculated values although the figure shows a sudden decrease of the measured beam density near the edge of the plasma (~ 3.7 m). This unexplained fall off was first observed by Mandl[20] and appears in the radial dependency of the measured beam density for all single beam bank pulses.

The time dependency of the measured and calculated neutral beam density for a typical pulse is shown in figure 5.17.

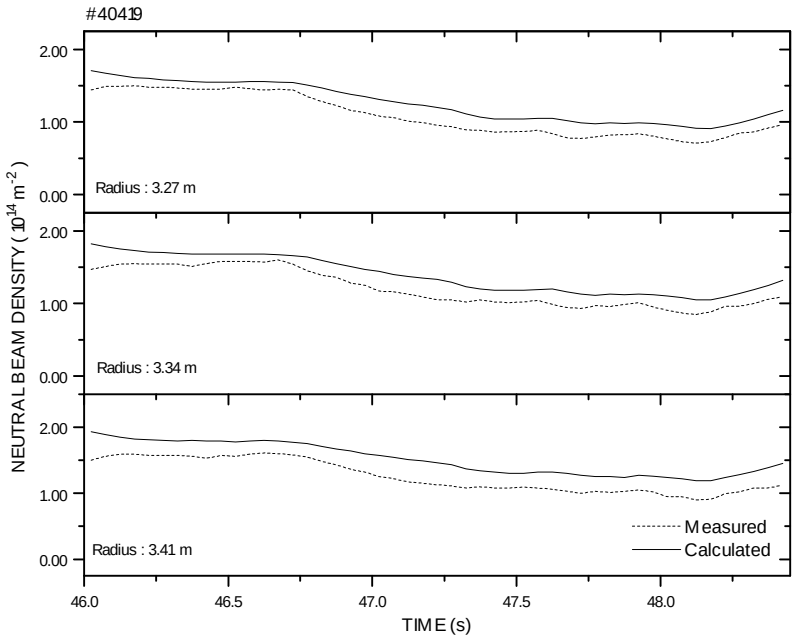

Figure 5.17 Time dependency of the measured and calculated neutral beam density for the single beam bank pulse 40419. Three radial positions have been selected to illustrate the results.

There is remarkably good agreement between the measured and calculated values at all times for the three different radial positions.

We also illustrate the pulse to pulse variation of the results. The criteria for the selection of pulses was simply that the pulses must have continuous neutral beam injection, see figure 5.18.

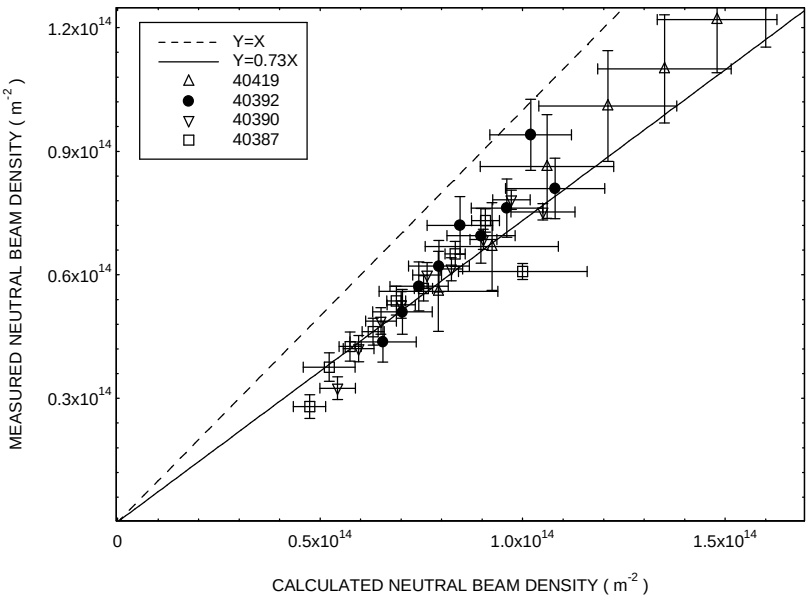

Figure 5.18 Variation of the measured and calculated beam density for a range of single beam bank pulses. Each data point represents a time averaged value for a fixed radial position. A measure of the deviation between the measured and calculated beam density is obtained by comparing the solid straight line with that of the dashed line which represents perfect agreement.

Each data point represents a time averaged value for a fixed radial position. The assigned error bar is simply the standard deviation associated with the time averaged value. A measure of the deviation between the measured and calculated beam density is obtained by comparing the solid straight line with that of the dashed line which represents perfect agreement. As shown in figure 5.18, an average difference of ~27 % can be observed between the measured and the calculated neutral beam density.

5.5.2 Double beam bank pulses

The radial dependence of the measure and calculated neutral beam density for a typical double beam bank pulse is shown in figure 5.19. Three time periods of the pulse have been selected to illustrate the results.

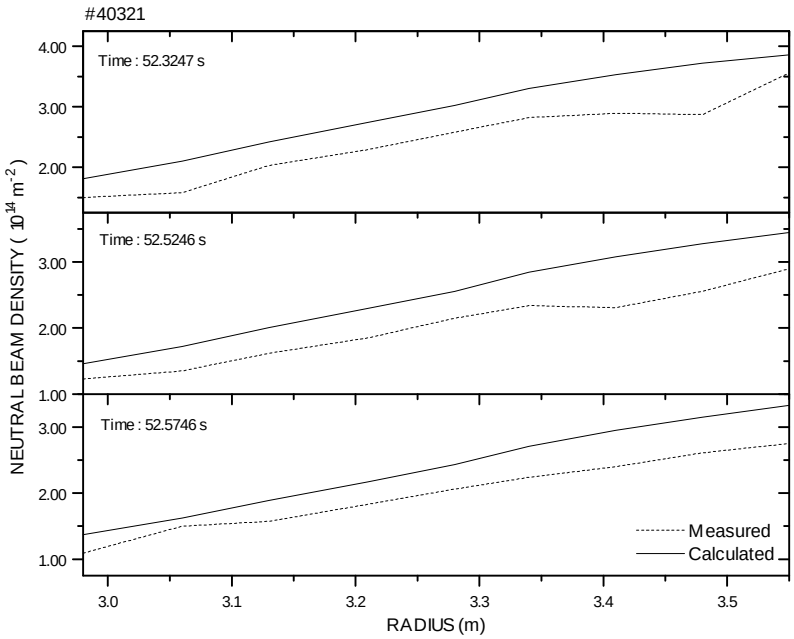

Figure 5.19 Radial dependence of the measured and calculated neutral beam density for three different time periods of the double beam bank pulse 40321.

The measured and calculated values show good agreement. However due to experimental difficulties we have no data near the edge of the plasma (~ 3.7 m), therefore we cannot confirm the fall off of the measured beam density as observed from the analysis of single beam bank spectra.

In figure 5.20 we show the time dependence of the measured and calculated values for three radial positions. We now consider the pulse to pulse variation between the measured and calculated neutral beam density. The selection criteria were the same as for single beam bank pulses. The results can be seen in figure 5.21, where an average difference of ~20 % can be observed between the measured and the calculated neutral beam density. It should be noted that each point represents a time averaged value for a fixed radial position.

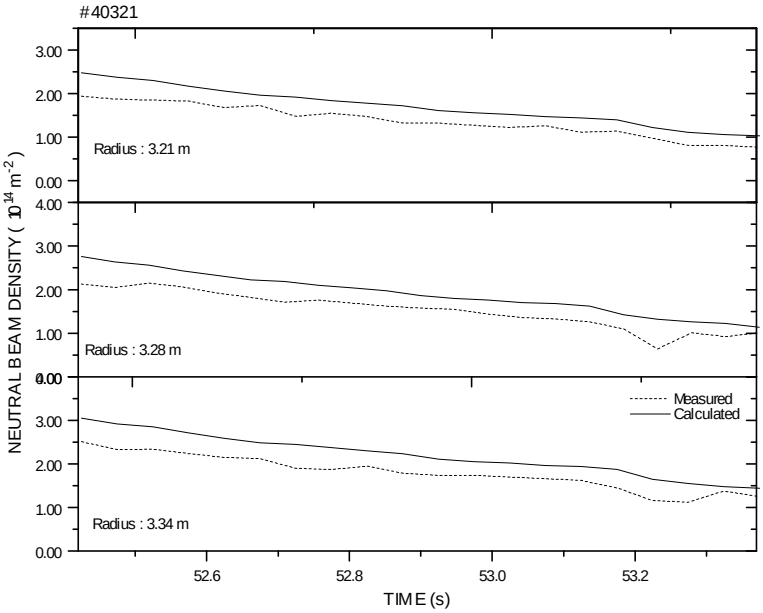

Figure 5.20 Time dependence of the measured and calculated neutral beam density at three radial positions for the double beam bank pulse 40321. Good agreement between the measured and calculated values as a function of time can clearly be observed.

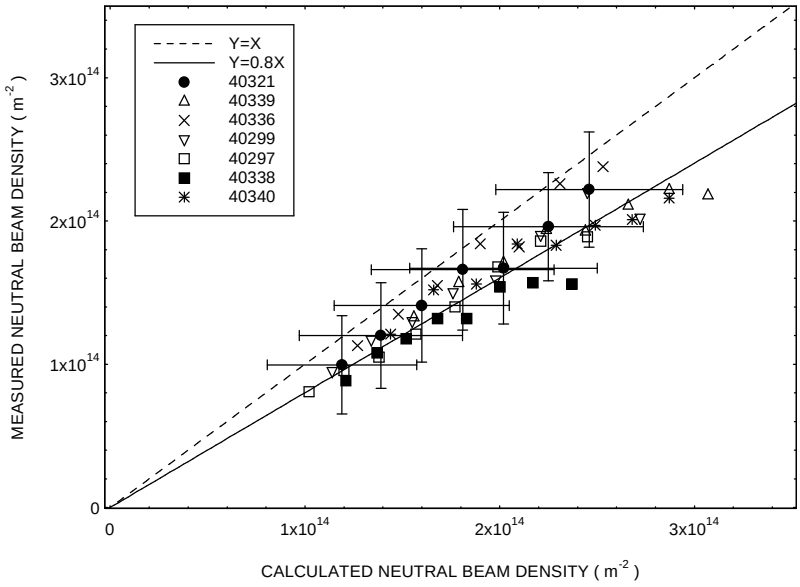

Figure 5.21 The variation between the measured and calculated neutral beam density for a range of double beam bank pulses. The solid straight line represents a line of best fit through the data points. A measure of the deviation between the measured and calculated beam density is obtained by comparing the solid straight line with that of the dashed line representing perfect agreement.

5.6 Conclusion

Refinements in the spectral fitting, consistency in the charge exchange analysis and the use of improved data which enters into the modelling to evaluate the effective coefficients, have led to the reliable deduction of the neutral beam density from the single and double beam bank spectra.

For single beam bank spectra we are able to recover a neutral beam density to within 27 % of the values obtained from the attenuation calculation. In the case of double beam bank pulses, we can recover the neutral beam density to within 20% of the numerical attenuation calculation.

In both single and double beam bank scenarios the time dependence between the measure and calculated beam density is remarkably good and this adds some credence to the atomic modelling. It should be noted however that from the results it appears that we can measure the beam density from double beam bank pulses with a greater accuracy than that for single beam bank pulses. This is some what surprising since the beam emission spectrum from a single beam bank pulse is much easier to analyse.

.